Advances in Applied Mathematics and Mechanics
Adv. Appl. Math. Mech., Vol. **8**, No. 2, pp. 306-330

DOI: 10.4208/aamm.2014.m672
April 2016

Rectangular Lattice Boltzmann Equation for Gaseous Microscale Flow

Junjie Ren[1], Ping Guo[2] and Zhaoli Guo[3,*]

[1] *School of Sciences, Southwest Petroleum University, Chengdu 610500, China*
[2] *State Key Laboratory of Oil and Gas Reservoir Geology and Exploitation, Southwest Petroleum University, Chengdu 610500, China*
[3] *State Key Laboratory of Coal Combustion, Huazhong University of Science and Technology, Wuhan 430074, China*

Received 25 June 2014; Accepted (in revised version) 26 January 2015

Abstract. The lattice Boltzmann equation (LBE) is considered as a promising approach for simulating flows of liquid and gas. Most of LBE studies have been devoted to regular square LBE and few works have focused on the rectangular LBE in the simulation of gaseous microscale flows. In fact, the rectangular LBE, as an alternative and efficient method, has some advantages over the square LBE in simulating flows with certain computational domains of large aspect ratio (e.g., long micro channels). Therefore, in this paper we expand the application scopes of the rectangular LBE to gaseous microscale flow. The kinetic boundary conditions for the rectangular LBE with a multiple-relaxation-time (MRT) collision operator, i.e., the combined bounce-back/specular-reflection (CBBSR) boundary condition and the discrete Maxwell's diffuse-reflection (DMDR) boundary condition, are studied in detail. We observe some discrete effects in both the CBBSR and DMDR boundary conditions for the rectangular LBE and present a reasonable approach to overcome these discrete effects in the two boundary conditions. It is found that the DMDR boundary condition for the square MRT-LBE can not realize the real fully diffusive boundary condition, while the DMDR boundary condition for the rectangular MRT-LBE with the grid aspect ratio $a \neq 1$ can do it well. Some numerical tests are implemented to validate the presented theoretical analysis. In addition, the computational efficiency and relative difference between the rectangular LBE and the square LBE are analyzed in detail. The rectangular LBE is found to be an efficient method for simulating the gaseous microscale flows in domains with large aspect ratios.

AMS subject classifications: 76M28, 76D05, 76P05

Key words: Lattice Boltzmann equation, gaseous microscale flow, rectangular lattice, boundary conditions, multiple-relaxation time.

*Corresponding author.
Email: renjunjie1900@126.com (J. Ren), guopingswpi@vip.sina.com (P. Guo), zlguo@hust.edu.cn (Z. Guo)

 ©2016 Global Science Press

https://doi.org/10.4208/aamm.2014.m672 Published online by Cambridge University Press

1 Introduction

The wide applications of micro-electro-mechanical-systems (MEMS) and nano-electro-mechanical-systems (NEMS) have stimulated a great interest in the development of simulation methods for gaseous microscale flow [1,2]. For non- continuum flows, the characteristic parameter is the Knudsen number $Kn=\lambda/h$, where λ represents the mean-free path of the gas and h is the characteristic length of the flow. According to the value of Kn, the flow can be classified into four flow regimes, i.e., the continuum flow ($Kn\leq 0.001$), the slip flow ($0.001<Kn\leq 0.1$), the transition flow ($0.1<Kn\leq 10$), and free molecular flow ($Kn>10$). Therefore, when Kn is greater than around 0.001, the continuum assumption will break down and the traditional simulation approaches based on the Navier-Stokes equations are not valid.

The lattice Boltzmann equation (LBE), which is a special discrete form of the continuous Boltzmann equation [3, 4], is considered as a promising method for simulating gaseous microscale flow [5]. Recently, numerous LBE studies have been devoted to gaseous microscale flow and most of them have focused on the LBE with a regular square lattice [6–25]. However, to our knowledge, there are few LBE works to study gaseous microscale flow based on a rectangular lattice. In fact, the rectangular LBE, as an alternative and efficient method, has some advantages over the square LBE for simulating flows in some cases.

Recently, the two-dimensional nine-velocity (D2Q9) LBE model with a rectangular lattice has been received particular attention and further studied [26–30]. As pointed out in [30], the rectangular LBE schemes can be constructed in three distinct approaches: the first method is to decouple the discretization of the velocity space from spatial and temporal discretizations [31], the second one is to construct a multiple-relaxation-time (MRT) operator [26], and the third one is to introduce some more discrete velocities [30]. Compared to the second approach mentioned above, the first approach loses the simplicity of the LBE and the third approach can not generate real rectangular grids. Therefore, in this work we choose the rectangular D2Q9 MRT-LBE model presented in [26] to study gaseous microscale flow.

The aim of this paper is to analyze two kinds of boundary conditions for the rectangular LBE and to apply the method to gaseous microscale flows in slip regime. The rest of the paper is organized as follows. In Section 2, we present the Chapman-Enskog analysis and derive the relationship between the relaxation parameter and the Knudsen number for the rectangular LBE model. In Section 3, we analyze the combined bounce-back/specular-reflection (CBBSR) boundary condition and the discrete Maxwells diffuse-reflection (DMDR) boundary condition for the rectangular LBE, and show how to choose the reasonable combination parameters (i.e., the bounce-back fraction for the CBBSR scheme and the accommodation coefficient for the DMDR scheme) in the two boundary conditions. In Section 4, the numerical tests are performed to validate the presented theoretical analysis. Finally, we conclude the paper in Section 5.

https://doi.org/10.4208/aamm.2014.m672 Published online by Cambridge University Press

2 Rectangular lattice Boltzmann equation

We consider the rectangular D2Q9 MRT-LBE model presented in [26]

$$f_i(\mathbf{r}+\mathbf{c}_i\delta_t,t+\delta_t)-f_i(\mathbf{r},t)=\Omega_i+\delta_t F'_i, \tag{2.1}$$

for $i=0,1,\cdots,8$, where f_i is the density distribution function associated with the molecular velocity $\mathbf{c}_i$ at position $\mathbf{r}=(x,y)$ and time t, δ_t is the time step, Ω_i is the discrete collision operator, F'_i is the discrete forcing term accounting for the external force $\mathbf{F}=(F_x,F_y)^{\mathrm{T}}$, and $\mathbf{c}_i$ is the molecular velocity, which is given by

$$\mathbf{c}_i=\begin{cases}(0,0), & i=0,\\ (\cos[(i-1)\pi/2],a\sin[(i-1)\pi/2])c, & i=1-4,\\ (\cos[(2i-9)\pi/4],a\sin[(2i-9)\pi/4])\sqrt{2}c, & i=5-8,\end{cases} \tag{2.2}$$

where $c=\delta_x/\delta_t$ (set to be 1 in this work), with δ_x and δ_t representing the lattice spacing in the x direction and the time step, respectively; $a=\delta_y/\delta_x$, where $0<a\leq 1$ is the aspect ratio of the rectangular grid, with δ_y representing the lattice spacing in the y direction.

The discrete collision operator in the rectangular D2Q9 MRT-LBE model is given by

$$\Omega_i=-\sum_{j=0}^{8}(\mathbf{M}^{-1}\mathbf{S}\mathbf{M})_{ij}\left[f_j-f_j^{(\mathrm{eq})}\right], \tag{2.3}$$

where $\mathbf{S}=\mathrm{diag}(s_0,s_1,s_2,s_3,s_4,s_5,s_6,s_7,s_8)$ is a diagonal relaxation matrix, $f_j^{(\mathrm{eq})}$ is the equilibrium distribution function, and $\mathbf{M}$ is the transformation matrix, which is given by [26]

$$\mathbf{M}=\begin{pmatrix}1&1&1&1&1&1&1&1&1\\ -2\varphi_1&\varphi_2&\varphi_3&\varphi_2&\varphi_3&\varphi_1&\varphi_1&\varphi_1&\varphi_1\\ 4&-2&-2&-2&-2&1&1&1&1\\ 0&1&0&-1&0&1&-1&-1&1\\ 0&-2&0&2&0&1&-1&-1&1\\ 0&0&a&0&-a&a&a&-a&-a\\ 0&0&-2a&0&2a&a&a&-a&-a\\ -2\varphi_4&\varphi_5&\varphi_6&\varphi_5&\varphi_6&\varphi_4&\varphi_4&\varphi_4&\varphi_4\\ 0&0&0&0&0&a&-a&a&-a\end{pmatrix}, \tag{2.4}$$

where $\varphi_1=a^2+1$, $\varphi_2=1-2a^2$, $\varphi_3=a^2-2$, $\varphi_4=a^2-1$, $\varphi_5=a^2+2$, and $\varphi_6=-(2a^2+1)$.

We can project the density distribution function f_i and the equilibrium distribution function $f_i^{(\mathrm{eq})}$ in velocity space onto macroscopic variables in moment space through the transformation matrix $\mathbf{M}$

$$\mathbf{m}:=\mathbf{M}\mathbf{f}=\left(\rho,e,\varepsilon,\rho u_x-\frac{\delta_t}{2}F_x,q_x,\rho u_y-\frac{\delta_t}{2}F_y,q_y,p_{xx},p_{xy}\right)^{\mathrm{T}}, \tag{2.5a}$$

$$\mathbf{m}^{(\mathrm{eq})}:=\mathbf{M}\mathbf{f}^{(\mathrm{eq})}=\left(\rho,e^{(\mathrm{eq})},\varepsilon^{(\mathrm{eq})},\rho u_x,q_x^{(\mathrm{eq})},\rho u_y,q_y^{(\mathrm{eq})},p_{xx}^{(\mathrm{eq})},p_{xy}^{(\mathrm{eq})}\right)^{\mathrm{T}}, \tag{2.5b}$$

https://doi.org/10.4208/aamm.2014.m672 Published online by Cambridge University Press

where $\mathbf{f}=(f_0,f_1,\cdots,f_8)^{\mathrm{T}}$, $\mathbf{f}^{(\mathrm{eq})}=(f_0^{(\mathrm{eq})},f_1^{(\mathrm{eq})},\cdots,f_8^{(\mathrm{eq})})^{\mathrm{T}}$, ρ is the density, u_x and u_y are the velocities in the x and y directions, F_x and F_y are the external forces in the x and y directions, e is related to the kinetic energy, ε is related to the kinetic energy squared for $a=1$ (but has no obvious physical meaning when $a\neq 1$), q_x and q_y are proportional to the x and y components of the energy flux, p_{xx} and p_{xy} are proportional to the diagonal and off-diagonal components of the viscous stress tensor, and $e^{(\mathrm{eq})}$, $\varepsilon^{(\mathrm{eq})}$, $q_x^{(\mathrm{eq})}$, $q_y^{(\mathrm{eq})}$, $p_{xx}^{(\mathrm{eq})}$ and $p_{xy}^{(\mathrm{eq})}$ are the equilibrium values of the non-conserved moments.

The density and velocities can be defined as follows

$$\rho=\sum_i f_i, \tag{2.6a}$$

$$\rho\mathbf{u}=\sum_i \mathbf{c}_i f_i+\frac{\delta_t}{2}\mathbf{F}, \tag{2.6b}$$

where $\mathbf{u}=(u_x,u_y)^{\mathrm{T}}$ and $\mathbf{F}=(F_x,F_y)^{\mathrm{T}}$.

For the collision process, the equilibrium values of the non-conserved moments can be proposed by [26]

$$e^{(\mathrm{eq})}=2(3c_s^2-1-a^2)\rho+3\rho(u_x^2+u_y^2), \qquad \varepsilon^{(\mathrm{eq})}=\frac{\rho}{2}, \tag{2.7a}$$

$$q_x^{(\mathrm{eq})}=\frac{c_2+4(1-a^2)}{2a^2}\rho u_x, \qquad q_y^{(\mathrm{eq})}=\frac{1}{2}c_2\rho u_y, \tag{2.7b}$$

$$p_{xx}^{(\mathrm{eq})}=\frac{(a^2-1)}{a^2}\left[3(a^2+1)c_s^2-2a^2\right]\rho+3\rho\left(a^2u_x^2-\frac{1}{a^2}u_y^2\right), \qquad p_{xy}^{(\mathrm{eq})}=\rho u_x u_y, \tag{2.7c}$$

where c_s is the sound speed, and c_2 is the coupling constant. It should be noted that for a given grid aspect ratio a $(a\neq 1)$, the values of c_s and c_2, which can optimize the isotropy and stability of the model, are not fixed but can be adjusted.

For the rectangular MRT-LBE model, the collision process is executed in moment space,

$$\widetilde{\mathbf{m}}(\mathbf{r},t)=\mathbf{m}(\mathbf{r},t)-\mathbf{S}\left[\mathbf{m}(\mathbf{r},t)-\mathbf{m}^{(\mathrm{eq})}(\mathbf{r},t)\right]+\delta_t\widehat{\mathbf{F}}, \tag{2.8}$$

and the propagation process is performed in velocity space,

$$f_i(\mathbf{r}+\mathbf{c}_i\delta_t,t+\delta_t)=\widetilde{f}_i(\mathbf{r},t), \tag{2.9}$$

where the quantities with and without the superscript "$\sim$" are the post-collision and pre-collision states, respectively. $\widehat{\mathbf{F}}=\mathbf{M}\mathbf{F}'$, with $\widehat{\mathbf{F}}=(\widehat{F}_0,\widehat{F}_1,\cdots,\widehat{F}_8)^{\mathrm{T}}$ and $\mathbf{F}'=(F'_0,F'_1,\cdots,F'_8)^{\mathrm{T}}$, can be directly chosen in moment space. We suggest

$$\widehat{F}_0=0, \qquad \widehat{F}_1=6\left(1-\frac{s_1}{2}\right)(u_xF_x+u_yF_y), \qquad \widehat{F}_2=-6\left(1-\frac{s_2}{2}\right)(u_xF_x+u_yF_y), \tag{2.10a}$$

$$\widehat{F}_3=\left(1-\frac{s_3}{2}\right)F_x, \qquad \widehat{F}_4=-\left(1-\frac{s_4}{2}\right)F_x, \qquad \widehat{F}_5=\left(1-\frac{s_5}{2}\right)F_y, \tag{2.10b}$$

$$\widehat{F}_6=-\left(1-\frac{s_6}{2}\right)F_y, \quad \widehat{F}_7=6\left(1-\frac{s_7}{2}\right)\left(a^2u_xF_x-\frac{1}{a^2}u_yF_y\right), \quad \widehat{F}_8=\left(1-\frac{s_8}{2}\right)(u_xF_y+u_yF_x), \tag{2.10c}$$

https://doi.org/10.4208/aamm.2014.m672 Published online by Cambridge University Press

which are similar to the discrete forcing terms of the square D2Q9 MRT-LBE model presented in [17,32].

Through the Chapman-Enskog analysis instead of the linear analysis presented in [26], we can derive the macroscopic equations from the rectangular LBE model (see Appendix for detail),

$$\partial_t\rho+\nabla\cdot(\rho\mathbf{u})=0, \tag{2.11a}$$

$$\partial_t(\rho\mathbf{u})+\nabla\cdot(\rho\mathbf{uu})=-\nabla p+\nabla\cdot[\rho\nu(\nabla\mathbf{u}+(\nabla\mathbf{u})^{\mathrm{T}}-(\nabla\cdot\mathbf{u})\mathbf{I})+\rho\zeta(\nabla\cdot\mathbf{u})\mathbf{I}]+\mathbf{F}+\mathbf{R}, \tag{2.11b}$$

where $p=\rho c_s^2$ is the pressure, $\mathbf{I}$ is the unit matrix, ν and ζ are the kinematic shear and bulk viscosities given by

$$\nu=\frac{4+c_2}{6}\Big(\frac{1}{s_8}-\frac{1}{2}\Big)\delta_t, \tag{2.12a}$$

$$\zeta=\frac{1}{12}(7+3a^2+c_2-12c_s^2)\Big(\frac{1}{s_1}-\frac{1}{2}\Big)\delta_t. \tag{2.12b}$$

Compared with the Navier-Stokes equations, the macroscopic equations from the rectangular LBE model include an additional term $\mathbf{R}$ given by

$$\mathbf{R}=\Big[\frac{a^2-1}{2}\Big(\frac{1}{s_1}-\frac{1}{2}\Big)\delta_t\partial_x(\rho\partial_y u_y),\ \frac{1-a^2}{2}\Big(\frac{1}{s_1}-\frac{1}{2}\Big)\delta_t\partial_y(\rho\partial_x u_x)\Big]^{\mathrm{T}}. \tag{2.13}$$

The additional term $\mathbf{R}$ probably means that, although the model presented [26] is Galilean invariant and isotropic up to the second order in the wave-vector $\mathbf{k}$, the hydrodynamic modes in the model differ from those in a real fluid by involving motions that are not exactly parallel or perpendicular to the wave-vector $\mathbf{k}$. Clearly, $\mathbf{R}=0$ as $a=1$, which is consistent with the square D2Q9 model [32].

Because of the constraints of the isotropy, the relaxation parameters are coupled by the following relationships [26]

$$\frac{1}{\widetilde{s}_1}=\frac{2(4+c_2)\big[(12c_s^2-c_2)(1+a^2)-2(5a^2+2)\big]}{(1+a^2)(1+c_2-3a^2)(c_2+10-12c_s^2)+6\big[a^4(c_2-2)-3(a^2-1)\big]}\frac{1}{\widetilde{s}_8}, \tag{2.14a}$$

$$\frac{1}{\widetilde{s}_7}=\frac{2(4+c_2)\big[(12c_s^2-c_2)(1+a^2)-2(3a^4+5a^2+5)\big]}{(1+a^2)(1+c_2-3a^2)(c_2+10-12c_s^2)+6\big[a^4(c_2-2)-3(a^2-1)\big]}\frac{1}{\widetilde{s}_8}, \tag{2.14b}$$

where $1/\widetilde{s}_\alpha=(1/s_\alpha-1/2)$. Note that the relationship between s_1 and s_8 is needed only when $a\neq1$.

It is important for us to consider two critical issues before we use the rectangular LBE model to simulate various flows. The first one is the numerical stability of the rectangular LBE model. As pointed out in [26], the stable region in parameter space of $\mathbf{u}$ and s_i for the rectangular LBE model is smaller than that for the square LBE model. Therefore, the rectangular LBE model limits ability to simulate flows even at moderate Reynolds

https://doi.org/10.4208/aamm.2014.m672 Published online by Cambridge University Press

numbers. Fortunately, the Reynolds number of gaseous microscale flow is usually small. Another critical issue is about the additional term **R** in the macroscopic equations from the rectangular LBE model. As shown in Eq. (2.13), for the model with a square grid $(a=1)$, or flows such as the Poiseuille flow satisfying $\partial_x(\rho\partial_y u_y)=0$ and $\partial_y(\rho\partial_x u_x)=0$, the additional term **R** in the macroscopic equations will disappear. Otherwise, the effect of the additional term **R** can be reduced by adjusting the values of c_s and c_2. In general cases, to eliminate the effect of the additional term **R**, we can absorb this term into the body force, i.e., in the evolution equation (2.8) we replace **F** with $\mathbf{F}-\mathbf{R}$.

Owing to the small Reynolds number of gaseous microscale flow, the rectangular D2Q9 LBE model can be competent for simulating gaseous microscale flow. For gaseous microscale flow, the characteristic parameter is the Knudsen number Kn. Therefore, the relationship between the relaxation parameter in the rectangular LBE and the Knudsen number must be given appropriately.

According to the gas kinetic theory, the relationship between the mean-free path λ and the dynamic viscosity $\mu=\rho\nu$ can be expressed by [33]

$$\lambda=\frac{\mu}{p}\sqrt{\frac{\pi RT}{2}}, \tag{2.15}$$

where R is the gas constant, and T is the system temperature.

Substituting Eq. (2.12a) and $p=\rho c_s^2=\rho RT$ into Eq. (2.15), we can obtain that

$$\lambda=\frac{4+c_2}{6}\sqrt{\frac{\pi}{2c_s^2}}\left(\frac{1}{s_8}-\frac{1}{2}\right)\delta_t. \tag{2.16}$$

Without loss of generality, here we consider that the characteristic length is aligned with the y-axis. Then, with the aid of Eq. (2.16), the relationship between s_8 and Kn is given by

$$\frac{1}{s_8}-\frac{1}{2}=aN_yKn\frac{6}{4+c_2}\sqrt{\frac{2c_s^2}{\pi}}, \tag{2.17}$$

where $N_y=h/\delta_y$ is the grid number in the direction of the characteristic length, and h is the characteristic length.

3 Kinetic boundary conditions for rectangular LBE

To obtain reasonable results, it is necessary to choose the suitable boundary condition in the process of simulating gaseous microscale flow. In practice, two types of kinetic boundary conditions, which are the combined bounce-back/specular- reflection (CBB-SR) scheme [34] and the discrete Maxwells diffuse-reflection (DMDR) scheme [35], are widely applied in LBE. Recently, the two kinetic boundary conditions for both square BGK- and MRT-LBE were analyzed, and it was found that both of them contain some

https://doi.org/10.4208/aamm.2014.m672 Published online by Cambridge University Press

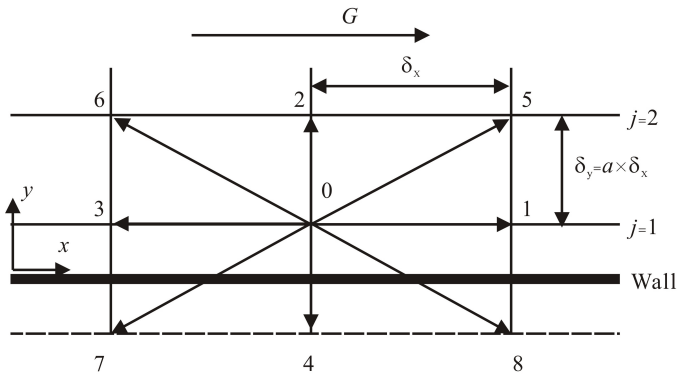


Figure 1: Lattice and boundary arrangement in the D2Q9 model with a rectangular lattice.

discrete effects and the combination coefficients should be chosen carefully under specified conditions [15–19, 22].

However, the aforementioned boundary conditions and the analysis focus only on the standard LBE model with a square lattice, and few works for the LBE model with a rectangular lattice have been studied. In what follows, we will investigate the two boundary conditions for the rectangular LBE.

For simplicity and without loss of generality, we consider a unidirectional gas flow over a stationary flat plate driven by a constant external acceleration G in the x direction (see Fig. 1), and we assume the gas flow satisfies the following conditions

$$\rho = const, \quad u_y = 0, \quad \frac{\partial \varphi}{\partial x} = 0, \quad \frac{\partial \varphi}{\partial t} = 0, \tag{3.1}$$

where φ is an arbitrary flow variable. As shown in Fig. 1, after the collision process at time t, the unknown distribution function, f_2^1, f_5^1, and f_6^1 at node $j=1$, can be determined by the CBBSR and DMDR boundary conditions, respectively:

$$\begin{cases} f_2^1 = \widetilde{f}_4^1, \\ f_5^1 = r\widetilde{f}_7^1 + (1-r)\widetilde{f}_8^1, \\ f_6^1 = r\widetilde{f}_8^1 + (1-r)\widetilde{f}_7^1, \end{cases} \tag{3.2}$$

for the CBBSR boundary condition, where $0 \le r \le 1$ is the combination parameter representing the bounce-back fraction, and

$$\begin{cases} f_2^1 = \sigma K f_2^{(\mathrm{eq})}(\mathbf{u}_w) + (1-\sigma)\widetilde{f}_4^1, \\ f_5^1 = \sigma K f_5^{(\mathrm{eq})}(\mathbf{u}_w) + (1-\sigma)\widetilde{f}_8^1, \\ f_6^1 = \sigma K f_6^{(\mathrm{eq})}(\mathbf{u}_w) + (1-\sigma)\widetilde{f}_7^1, \end{cases} \tag{3.3}$$

for the DMDR boundary condition, where $0 \le \sigma \le 1$ is the combination coefficient (accommodation coefficient) representing the portion of particles fully diffused by the wall, K

https://doi.org/10.4208/aamm.2014.m672 Published online by Cambridge University Press

is defined as $K=(\widetilde{f}_4^1+\widetilde{f}_7^1+\widetilde{f}_8^1)/[f_2^{(\mathrm{eq})}(\mathbf{u}_w)+f_5^{(\mathrm{eq})}(\mathbf{u}_w)+f_6^{(\mathrm{eq})}(\mathbf{u}_w)]$, and $\mathbf{u}_w=0$ is the wall velocity. It should be noted that unlike the square LBE [15], for the rectangular LBE with the grid aspect ratio $a\neq 1$, the DMDR boundary condition can easily be applied to the moving boundaries [11], while it is unclear how to deal with such moving boundaries by the CBBSR boundary condition.

Following the method proposed in [15–17], we can obtain the following equation

$$u_x^{(2)}=Au_x^{(1)}+B\delta_t G, \tag{3.4}$$

where $u_x^{(1)}$ and $u_x^{(2)}$ are the velocities in the x direction at j=1 and j=2, and the parameters A and B are given by

$$A=\frac{1+2r(1/s_8-2)-2/s_8}{1+2r(1/s_8-1)-2/s_8}, \tag{3.5a}$$

$$B=\frac{2a^2}{4+c_2}\frac{6(2/s_8-1)+r[11-16/s_8+(8/s_8-4)/s_4]}{(2/s_8-1)[1-2/s_8+2r(1/s_8-1)]}, \tag{3.5b}$$

for the CBBSR boundary condition, and

$$A=\frac{1+\sigma(1/s_8-2)-2/s_8}{1+\sigma(1/s_8-1)-2/s_8}, \tag{3.6a}$$

$$B=\frac{2a^2}{4+c_2}\frac{6(2/s_8-1)+\sigma[11/2-8/s_8+(4/s_8-2)/s_4]}{(2/s_8-1)[1-2/s_8+\sigma(1/s_8-1)]}, \tag{3.6b}$$

for the DMDR boundary condition.

The discrete velocities at the inner node j satisfy the following equation

$$\nu\frac{u_x^{(j+1)}-2u_x^{(j)}+u_x^{(j-1)}}{\delta_y^2}+G=0, \tag{3.7}$$

which is just a second-order finite difference equation of the following partial differential equation

$$\nu\frac{\partial^2 u_x}{\partial y^2}+G=0. \tag{3.8}$$

In order to solve the finite difference equation (3.7), we need another boundary condition. Here, the Poiseuille flow with two walls located at $y=0$ and $y=H$ is considered. For this flow, the solution of Eq. (3.7) can be obtained as follows

$$u_x^{(j)}=4u_c\frac{y_j}{H}\left(1-\frac{y_j}{H}\right)+u_s, \tag{3.9}$$

where $y_j=(j-1/2)\delta_y$, $u_c=GH^2/(8\nu)$ and u_s is the slip velocity.

https://doi.org/10.4208/aamm.2014.m672 Published online by Cambridge University Press

Substituting Eq. (3.9) into Eq. (3.4), we can obtain that

$$U_s := \frac{u_s}{u_c} = \begin{cases} \dfrac{2(1-r)(2/s_8-1)}{r}\Delta + \dfrac{1}{3}[16/(s_4s_8)-8/s_8-8/s_4+1]\Delta^2 & \text{for CBBSR,} \\ \dfrac{2(2-\sigma)(2/s_8-1)}{\sigma}\Delta + \dfrac{1}{3}[16/(s_4s_8)-8/s_8-8/s_4+1]\Delta^2 & \text{for DMDR,} \end{cases} \tag{3.10}$$

where $\Delta = \delta_y/H$. With the aid of Eq. (2.17), Eq. (3.10) can be rewritten as

$$U_s = \begin{cases} \dfrac{24a\sqrt{c_s^2}(1-r)}{(4+c_2)r}\sqrt{\dfrac{2}{\pi}}Kn + \dfrac{96a^2c_s^2[16/(s_4s_8)-8/s_8-8/s_4+1]}{(4+c_2)^2\pi(1-2/s_8)^2}Kn^2 & \text{for CBBSR,} \\ \dfrac{24a\sqrt{c_s^2}(2-\sigma)}{(4+c_2)\sigma}\sqrt{\dfrac{2}{\pi}}Kn + \dfrac{96a^2c_s^2[16/(s_4s_8)-8/s_8-8/s_4+1]}{(4+c_2)^2\pi(1-2/s_8)^2}Kn^2 & \text{for DMDR.} \end{cases} \tag{3.11}$$

The second-order slip condition is widely used for the non-continuum gas flow and the slip velocity u_s can be obtained by

$$u_s = A_1\lambda\frac{\partial u_x}{\partial y}\Big|_{\text{wall}} - A_2\lambda^2\frac{\partial^2 u_x}{\partial y^2}\Big|_{\text{wall}}, \tag{3.12}$$

where A_1 and A_2 are the slip parameters relating to the gas-wall interaction. For a fully diffusive boundary, $A_1 = 2\xi/\sqrt{\pi}$ and $A_2 = (1+2\xi^2)/\pi$ with $\xi = 1.016$, are proposed by Cercignani [33]. By solving the Navier-Stokes equations with the boundary condition (3.12) for the Poiseuille flow, we can obtain the slip velocity at the wall as

$$U_s = 4A_1Kn + 8A_2Kn^2. \tag{3.13}$$

By comparing Eq. (3.11) with Eq. (3.13), we can find that in order to realize the second-order slip condition (3.12), the parameter r in CBBSR boundary condition (or σ in DMDR boundary condition) and the relaxation parameter s_4 must be chosen as follows

$$r = \frac{\sigma}{2} = \left[1 + \frac{(4+c_2)}{6a\sqrt{c_s^2}}\sqrt{\frac{\pi}{2}}A_1\right]^{-1}, \quad s_4 = \left[\frac{1}{2} + \frac{(4+c_2)^2\pi A_2(2/s_8-1)^2 + 36a^2c_s^2}{96a^2c_s^2(2/s_8-1)}\right]^{-1}. \tag{3.14}$$

It can be seen that when $a=1$, $c_s^2=1/3$, and $c_2=-2$, the above results coincide with the previous results for the square MRT-LBE [17]. However, it should be noted that unlike the square MRT-LBE [17], for the rectangular MRT-LBE with a given value of $a \neq 1$, the combination parameters r and σ in the two kinetic boundary conditions are not constants but depend on c_s and c_2. Therefore, by adjusting the values of c_s and c_2 so that both $0 \leq r \leq 1$ and $0 \leq \sigma \leq 1$, we can use both the CBBSR and DMDR boundary conditions to realize the real fully diffusive boundary condition, which is not realized by the DMDR boundary condition in the square MRT-LBE [17]. However, it should be noted that in general the stability of the rectangular LBE reduces with the grid aspect ratio a. Therefore, in order to obtain good numerical stability, the grid aspect ratio a will be set larger than or equal to 0.4 in the following simulations.

https://doi.org/10.4208/aamm.2014.m672 Published online by Cambridge University Press

4 Numerical tests

First, we validate the theoretical results by applying the rectangular MRT-LBE with the CBBSR and DMDR boundary conditions to the Poiseuille flow driven by a constant external acceleration $G=10^{-5}$. The flow considered is in a channel with the ratio of the length L to the height H being 10, and it is simulated by the rectangular LBE with several different values of the grid aspect ratio a. In order to compare with the square MRT-LBE model, we fix the grid number in the direction of the characteristic length ($N_y=36$) and choose the grid number in the x direction according to a. It is clear that compared with the square MRT-LBE model, the rectangular LBE model needs fewer grids in the x direction in the same computational domain. Periodic boundary conditions are applied to the inlet and outlet of the channel, and the CBBSR or DMDR boundary conditions are applied to the channel walls. For a given value of $a\neq 1$, the values of c_s and c_2 must be chosen such that the numerical stability of the model is satisfied and Eq. (3.14) leads to the parametric limitations ($0\leq r\leq 1$ and $0\leq\sigma\leq 1$). In general, to gain the numerical stability of the model, the values of c_s and c_2 can be chosen according to the linear analysis presented in [26]. These values are summarized in Table 1. The relaxation parameters are given as follows: s_8 is determined by Eq. (2.17), s_1 and s_7 are given by Eqs. (2.14a) and (2.14b) respectively, s_4 is obtained according to Eq. (3.14), s_0, s_3 and s_5 are related to the conserved quantities and are set to be 0, and the other two parameters are chosen to be $s_2=1.2$ and $s_6=s_4$. In the following simulations, the convergence criterion toward a steady state is set as follows:

$$\sqrt{\frac{\sum_{i,j}\left\{\left[u_x(i,j,t+100\delta_t)-u_x(i,j,t)\right]^2+\left[u_y(i,j,t+100\delta_t)-u_y(i,j,t)\right]^2\right\}}{\sum_{i,j}\left[u_x(i,j,t+100\delta_t)^2+u_y(i,j,t+100\delta_t)^2\right]}}<10^{-9}. \tag{4.1}$$

In Fig. 2, the slip velocities of the CBBSR and DMDR boundary conditions in the rectangular LBE model are measured as a function of r and σ. It is seen that the numerical predictions are in good agreement with the analytical results given by Eq. (3.11) for different grid aspect ratio a. Therefore, the choice of r and σ is important to obtain the reasonable slip velocity in simulations.

The discrete effects in the CBBSR and DMDR boundary conditions for the rectangular

Table 1: Simulation parameters of the micro-channel flows with different grid aspect ratios.

a	c_s	c_2	r	σ
1.00	$1/\sqrt{3}$	-2	0.5464	–
0.80	0.58	-0.9	0.3846	0.7692
0.65	0.48	-1.7	0.3616	0.7232
0.50	0.38	-2.5	0.3460	0.6920
0.45	0.34	-3.0	0.3898	0.7796
0.40	0.30	-3.2	0.3851	0.7702

https://doi.org/10.4208/aamm.2014.m672 Published online by Cambridge University Press

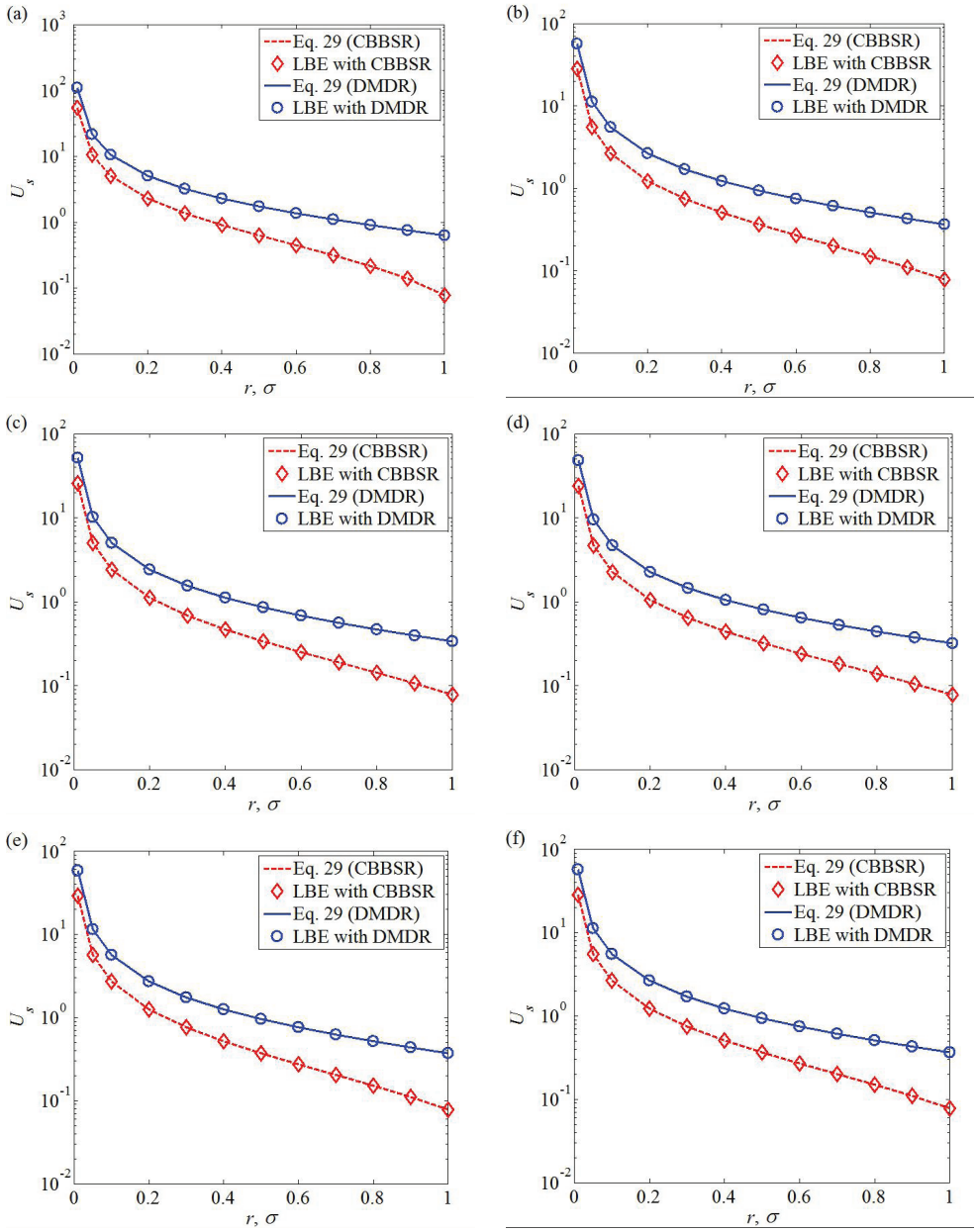


Figure 2: Slip velocity as functions of r and σ for the CBBSR and DMDR boundary conditions with $Kn=0.1$ and different values of the grid aspect ratio a. (a) $a=1.0$; (b) $a=0.8$; (c) $a=0.65$; (d) $a=0.5$; (e) $a=0.45$; (f) $a=0.4$.

LBE will be tested with different values of the grid aspect ratio a. In Fig. 3, the velocity profiles for the Poiseuille flow at $Kn=0.1$ for a fully diffusive wall are predicted by the rectangular LBE with the CBBSR boundary condition and different values of the grid

https://doi.org/10.4208/aamm.2014.m672 Published online by Cambridge University Press

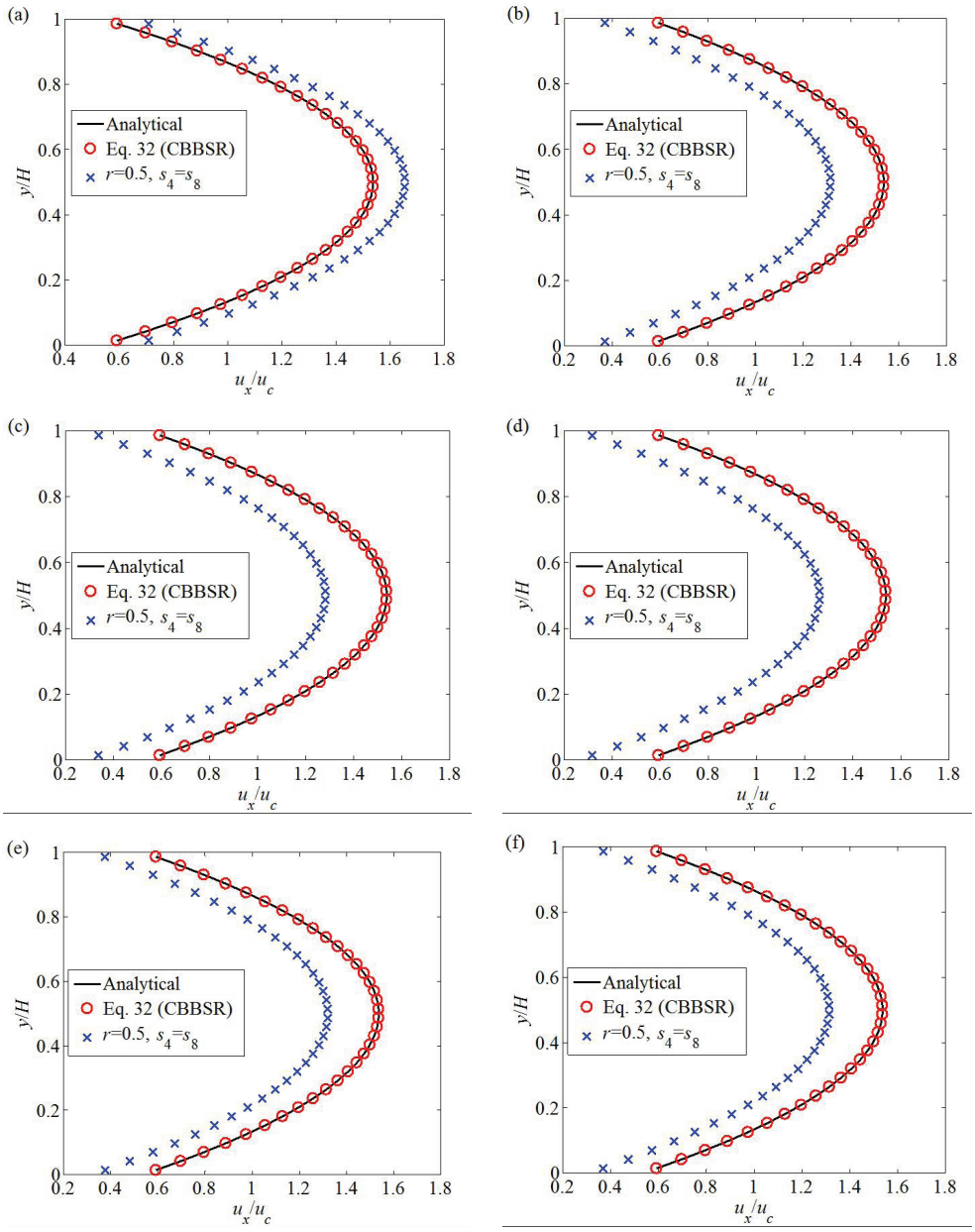


Figure 3: Velocity profiles for the Poiseuille flow at $Kn=0.1$ for a fully diffusive wall with the CBBSR boundary condition and different values of the grid aspect ratio a. (a) $a=1.0$; (b) $a=0.8$; (c) $a=0.65$; (d) $a=0.5$; (e) $a=0.45$; (f) $a=0.4$.

aspect ratio a. It can be seen that the results with the boundary condition considering the discrete effects, i.e., setting r and s_4 as Eq. (3.14), are in excellent agreement with the

https://doi.org/10.4208/aamm.2014.m672 Published online by Cambridge University Press

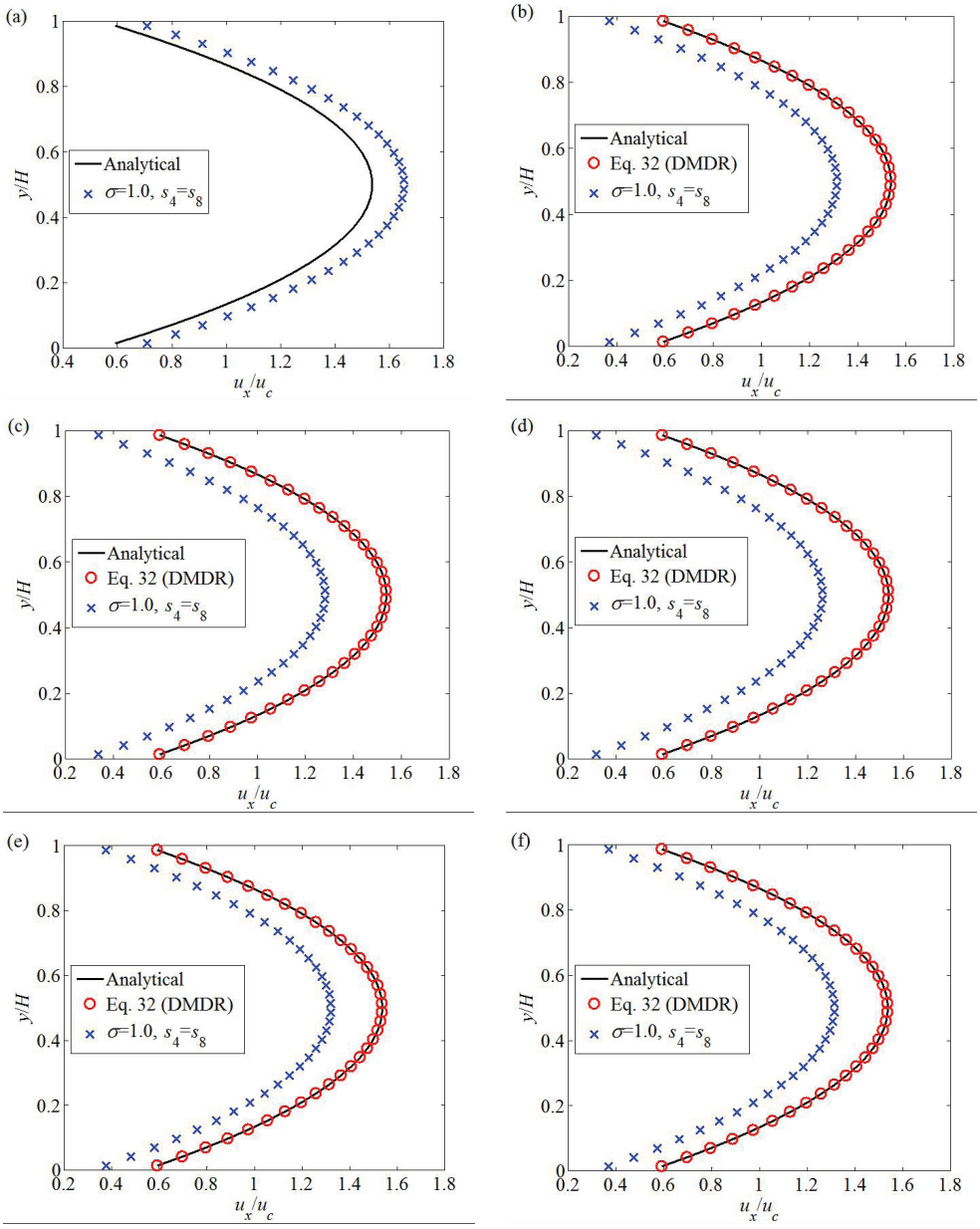


Figure 4: Velocity profiles for the Poiseuille flow at $Kn=0.1$ for a fully diffusive wall with the DMDR boundary condition and different values of the grid aspect ratio a. (a) $a=1.0$; (b) $a=0.8$; (c) $a=0.65$; (d) $a=0.5$; (e) $a=0.45$; (f) $a=0.4$.

analytic solutions in all cases, while those without considering the discrete effects, i.e., setting $r=0.5$ and $s_4=s_8$, deviate significantly from the analytic velocity profiles.

In Fig. 4, the same case is predicted by the rectangular LBE with the DMDR boundary

https://doi.org/10.4208/aamm.2014.m672 Published online by Cambridge University Press

condition and different values of the grid aspect ratio a. It is shown that the results with the boundary condition considering the discrete effects, i.e., setting σ and s_4 as Eq. (3.14), are also in excellent agreement with the analytic solutions in the case of $a\neq 1$, while those without considering the discrete effects, i.e., setting $\sigma=1.0$ and $s_4=s_8$, also deviate apparently from the analytic velocity profiles. Moreover, it should be noted that the DMDR boundary condition of the square MRT-LBE model does not realize the real fully diffusive boundary condition [17], while the DMDR boundary condition of the rectangular LBE model with $a\neq 1$ can successfully work in this case.

In what follows, the computational efficiency and numerical accuracy between the rectangular LBE and the square LBE in simulations are analyzed in detail. It is known that the running time of the LBE program is proportional to the product of the grid number ($N_x\times N_y$) and the iteration number (IN). Therefore, the relative running time (RRT) $\psi_{time}=T/T_s$, where $T=N_x\times N_y\times \text{IN}$ and the subscript s denotes "square LBE", is introduced to evaluate the computational efficiency between the rectangular LBE and the square LBE. With regard to the difference between the rectangular LBE and the square LBE, the relative global difference (RGD) $E_u=\|u(y)-u_s(y)\|/\|u_s(y)\|$ is assessed, where the norm is defined as $\|u(y)\|=[\sum_y u^2(y)]^{1/2}$. The comparison between the rectangular LBE and the square LBE for the Poiseuille flow at $Kn=0.1$ with $L/H=10$ is presented in Table 2, from which we can see that, compared with the square LBE, the rectangular LBE can obtain the same results but needs much less computation time. The comparison also demonstrates that the simulations are in good agreement with the theoretical analysis presented above, that is, for the LBE model with a square grid $(a=1)$, or flows such as the Poiseuille flow satisfying $\partial_x(\rho\partial_y u_y)=0$ and $\partial_y(\rho\partial_x u_x)=0$, the additional term $\mathbf{R}$ in the macroscopic equations will disappear.

Our second test case is the pressure-driven gas flow in a long microchannel with pressure boundary condition, which satisfies $\partial_x(\rho\partial_y u_y)\neq 0$ and $\partial_y(\rho\partial_x u_x)\neq 0$. To compare the simulation results with the direct simulation Monte Carlo (DSMC) and the information preservation (IP) results [36], the ratio of the length to the height of the channel is taken as $L/H=100$, the ratio of the inlet and outlet pressure is set to be $p_{in}/p_{out}=1.4$, and the Knudsen number at the outlet is fixed at $Kn_{out}=0.0194$. The local Knudsen number varies along the channel and can be calculated by $Kn(x)=Kn_{out}p_{out}/p(x)$, where $p(x)$ is the local pressure. The CBBSR boundary condition presented above is applied at the

Table 2: Computational efficiency and difference between the rectangular LBE and the square LBE for the Poiseuille flow at $Kn=0.1$ with $L/H=10$.

a	$N_x\times N_y$	IN	ψ_{time}	E_u
1.00	360×36	2600	1.000	0
0.80	288×36	2100	0.646	0
0.65	234×36	2000	0.500	0
0.50	180×36	2000	0.385	0
0.45	162×36	2000	0.346	0
0.40	144×36	2000	0.308	0

https://doi.org/10.4208/aamm.2014.m672 Published online by Cambridge University Press

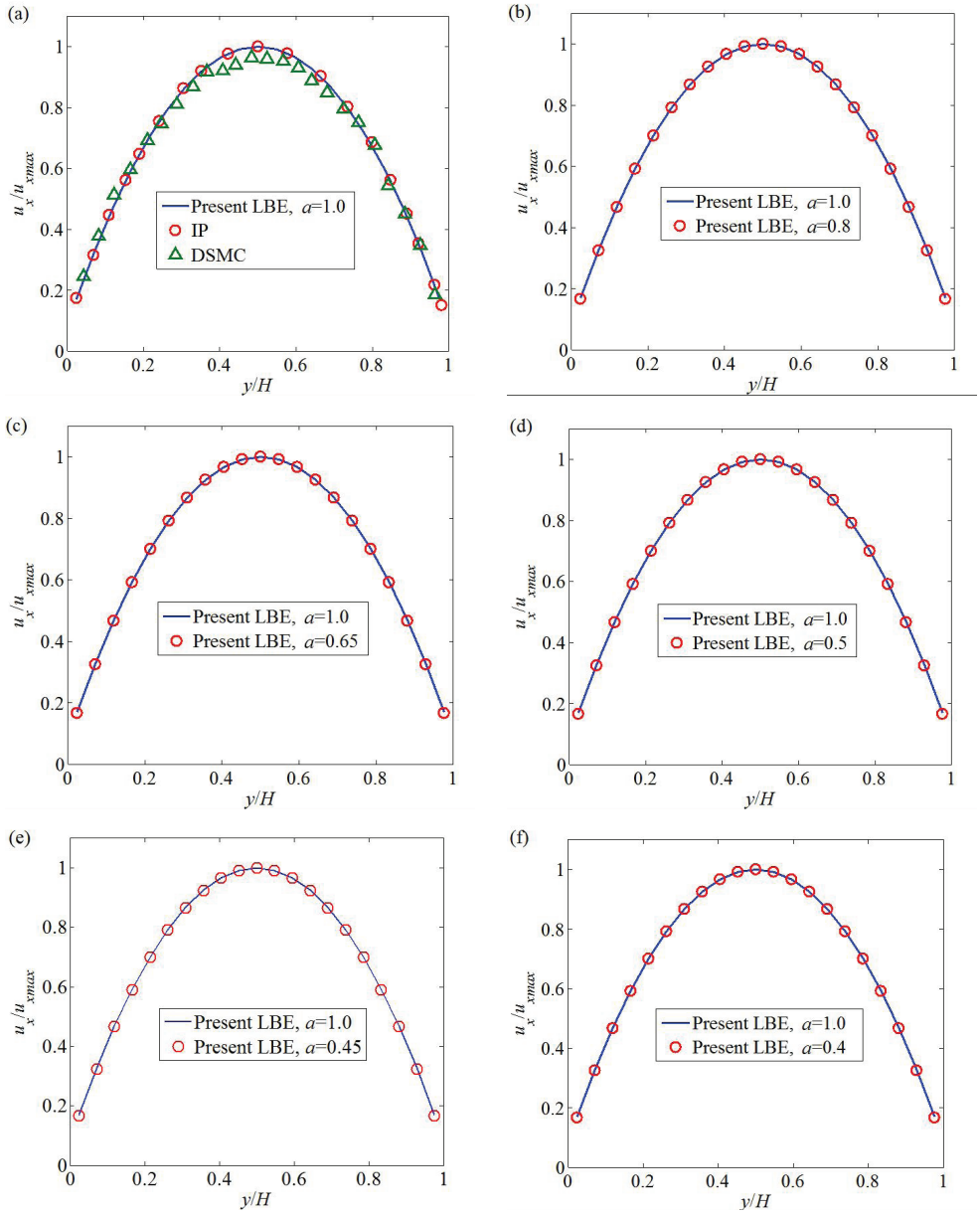


Figure 5: Streamwise velocity at the outlet for pressure-driven flow in a long microchannel with $Kn_{out}=0.0194$ and $p_{in}/p_{out}=1.4$. Comparison of the simulation results by the square LBE ($a=1.0$) with the results of IP and DSMC method [36] (a), and the simulation results by the rectangular LBE with $a=0.8$ (b), $a=0.65$ (c), $a=0.5$ (d), $a=0.45$ (e), and $a=0.4$ (f).

channel walls. The linear extrapolation scheme [20, 23] is adopted to realize the pressure boundary condition at the inlet and outlet. The grid number in the direction of the char-

https://doi.org/10.4208/aamm.2014.m672 Published online by Cambridge University Press

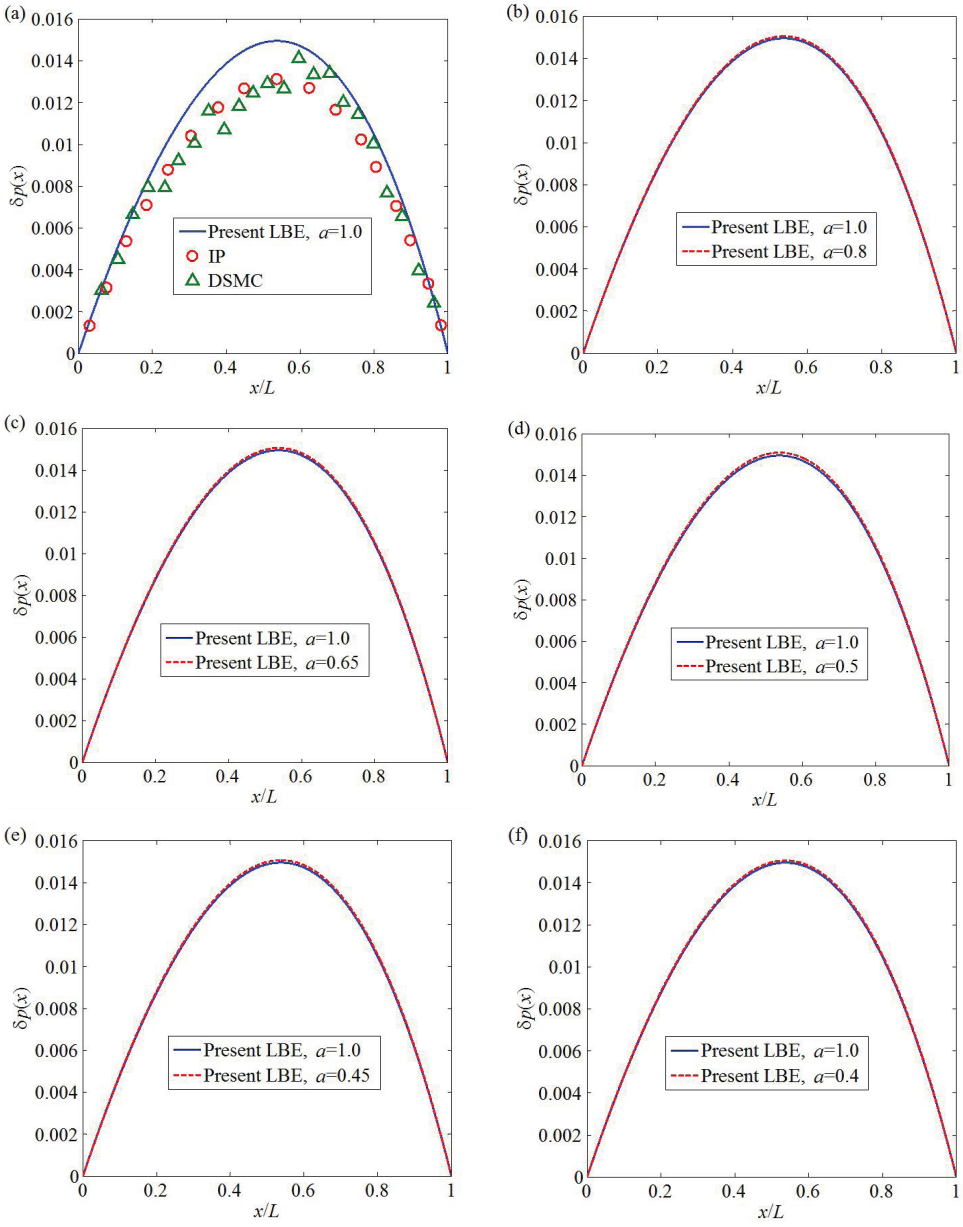


Figure 6: Pressure deviation along the centerline of the channel for pressure-driven flow in a long microchannel with $Kn_{out}=0.0194$ and $p_{in}/p_{out}=1.4$. Comparison of the simulation results by the square LBE ($a=1.0$) with the results of IP and DSMC method [36] (a), and the simulation results by the rectangular LBE with $a=0.8$ (b), $a=0.65$ (c), and $a=0.5$ (d), $a=0.45$ (e), and $a=0.4$ (f).

acteristic length is set to be $N_y=21$, which is able to obtain grid-independent results for the square LBE [23,37,38]. The grid number in the x direction can be given based on the

https://doi.org/10.4208/aamm.2014.m672 Published online by Cambridge University Press

Table 3: Computational efficiency and difference between the rectangular LBE and the square LBE for the pressure-driven flow in a long microchannel with $Kn_{out}=0.0194$ and $p_{in}/p_{out}=1.4$.

a	$N_x\times N_y$	IN	ψ_{time}	E_u
1.00	2100×21	82600	1.000	0
0.80	1680×21	67200	0.651	2.35×10^{-3}
0.65	1365×21	66000	0.519	2.37×10^{-3}
0.50	1050×21	64400	0.390	2.87×10^{-3}
0.45	945×21	64600	0.352	2.59×10^{-3}
0.40	840×21	65000	0.315	2.09×10^{-3}

value of the grid aspect ratio a. The values of c_s and c_2 for the rectangular LBE are shown in Table 1.

The streamwise velocity at the outlet and the pressure deviation along the centerline of the channel for pressure-driven flow in a long microchannel with $Kn_{out}=0.0194$ and $p_{in}/p_{out}=1.4$ are shown in Figs. 5 and 6, respectively, in which the IP and DSMC results [36] and the results obtained by the rectangular LBE with different grid aspect ratio a are presented for comparison. In Figs. 5 and 6, the dimensionless streamwise velocity $u_x/u_{x\max}$ at the outlet and the pressure deviation $\delta p(x)=[p(x)-p_l(x)]/p_{out}$ along the centerline of the channel are presented, where $u_{x\max}$ is the maximum velocity at the outlet and the linear distributed pressure $p_l(x)=p_{in}+x(p_{out}-p_{in})/L$. Figs. 5 and 6 show that the results by the rectangular LBE with $a\neq 1$ are in good agreement with the IP and DSMC results and the results by the square LBE.

The computational efficiency and difference between the rectangular LBE and the square LBE for the pressure-driven flow in a long microchannel with $Kn_{out}=0.0194$ and $p_{in}/p_{out}=1.4$ are listed in Table 3. From the table it is seen that in comparison with the square LBE, the rectangular LBE can effectively reduce the running time of the LBE program and can obtain the satisfactory numerical results. For instance, the RGD between the rectangular LBE with $a=0.5$ and the square LBE is 2.87×10^{-3}, and the RRT between the rectangular LBE with $a=0.5$ and the square LBE is only 0.390, indicating the rectangular LBE has a higher computational efficiency than the square LBE for the problem under nearly the same accuracy.

In addition, we also make some discussions on the effect of the values of c_s and c_2 on the computational efficiency and difference between the rectangular LBE and the square LBE for the pressure-driven flow in a long microchannel. Taking the rectangular LBE with $a=0.5$ for example, we use different values of c_s and c_2 to simulate the pressure-driven flow in a long microchannel with $Kn_{out}=0.0194$ and $p_{in}/p_{out}=1.4$. The results are listed in Table 4. From the table it is seen that the computational efficiency (ψ_{time}) and difference (E_u) are dependent on the choice of c_s and c_2, meaning that we can adjust the values of c_s and c_2 in the rectangular LBE to achieve a better balance between the accuracy and efficiency. The detailed study of the effect of c_s and c_2 on the accuracy and efficiency is very complex and beyond the scope of the present work.

Our third test problem is the micro-lid-driven cavity flow. The flow is contained in a

https://doi.org/10.4208/aamm.2014.m672 Published online by Cambridge University Press

Table 4: Effect of c_s and c_2 on the computational efficiency and difference between the rectangular LBE with $a=0.5$ and the square LBE for the pressure-driven flow in a long microchannel with $Kn_{out}=0.0194$ and $p_{in}/p_{out}=1.4$.

a	c_s	c_2	r	σ	$N_x\times N_y$	IN	ψ_{time}	E_u
0.50	0.45	-2.5	0.3851	0.7702	1050×21	55500	0.336	7.62×10^{-3}
0.50	0.38	-2.5	0.3460	0.6920	1050×21	64400	0.390	2.87×10^{-3}
0.50	0.377	-2.55	0.3519	0.7038	1050×21	64800	0.392	2.61×10^{-3}
0.50	0.36	-2.5	0.3338	0.6676	1050×21	67500	0.409	1.00×10^{-3}
0.50	0.35	-2.5	0.3276	0.6552	1050×21	69100	0.418	4.53×10^{-5}
0.50	0.35	-3.2	0.4774	0.9548	1050×21	69000	0.418	5.04×10^{-5}
0.50	0.34	-2.5	0.3212	0.6424	1050×21	70900	0.429	1.18×10^{-3}
0.50	0.33	-2.5	0.3148	0.6296	1050×21	72700	0.440	2.42×10^{-3}

cavity with $L/H=3$, where L is the cavity width and H is the cavity depth. The upper wall of the cavity moves with a constant velocity U from left to right, and the other three walls of the cavity are stationary. In simulations, the Reynolds number Re, where $Re=UH/\nu$, is taken as 0.3, the Knudsen number Kn is set to be 0.01, and the grid number in the direction of the characteristic length is fixed at $N_y=255$. In order to make the vertical centerline of the cavity on the grid points, we choose the rectangular LBE with $N_x=459$ ($a=0.6$) to simulate the flow. Because the DMDR scheme of the square LBE can not realize the real fully diffusive boundary condition and the CBBSR scheme of the rectangular LBE with $a\neq1$ can not be employed in dealing with the moving boundaries, to realize the real fully diffusive boundary condition, we use the DMDR scheme at all solid walls for the rectangular LBE with $a\neq1$ and apply the CBBSR scheme with moving boundaries [15] to the solid walls for the square LBE. In order to gain good stability, the values of c_s and c_2 for the rectangular LBE with $a=0.6$ are chosen as 0.44 and -2.0, respectively.

Fig. 7 shows the results of the rectangular LBE with $a=0.6$, which are in good agreement with those of the square LBE. It can be seen that the rectangular LBE [26] can be used to simulate the cavity flow which is always considered as a severe test to demonstrate the isotropy of the model. The RGD and the RRT between the rectangular LBE with $a=0.6$ and the square LBE are $E_u=4.5\times10^{-3}$ and $\psi_{time}=0.466$, respectively, which indicates the rectangular LBE with $a=0.6$ is of higher efficiency with nearly the same accuracy.

As mentioned above, to recover the macroscopic equations more accurately, we can also improve the rectangular LBE model by replacing $\mathbf{F}$ with $\mathbf{F}-\mathbf{R}$ in the evolution equation (2.8). It should be noted that although the improved rectangular LBE can accurately recover the Navier-Stokes equations by the Chapman-Enskog analysis, it will introduce the density and velocity gradients in the LBE, which may affect the numerical stability and the computational efficiency of the LBE. Finally, we will make a comparison between the improved rectangular LBE and the previous one by simulating the micro-lid-driven cavity flow mentioned above.

https://doi.org/10.4208/aamm.2014.m672 Published online by Cambridge University Press

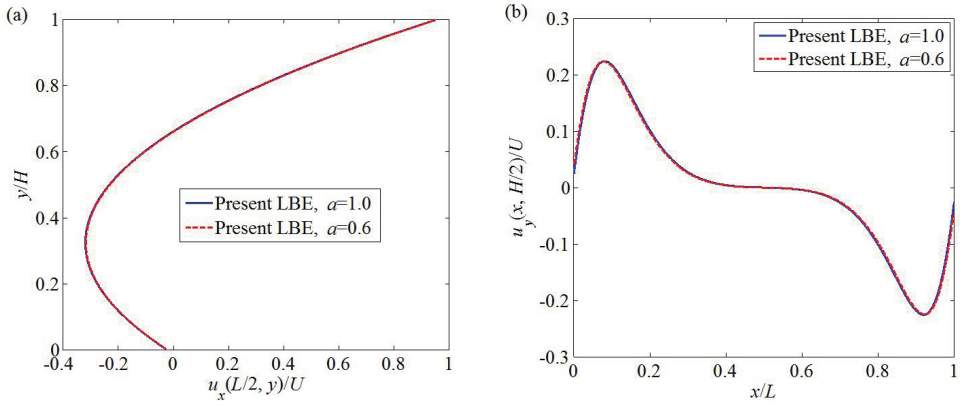


Figure 7: The velocity profiles across the cavity center at $Re=0.3$ and $Kn=0.01$. (a) streamwise velocity along the vertical centerline. (b) spanwise velocity along the horizontal centerline.

In order to make the comparison under the same conditions, the same values of c_s and c_2 should be used in both the improved rectangular LBE and the previous one. It should be noted that compared with the previous rectangular LBE, the values of c_s and c_2 for the improved rectangular LBE will be chosen in a narrower range, which may be because introducing the density and velocity gradients in the LBE will affect the numerical stability. To gain good stability of both the improved rectangular LBE and the previous one, the values of c_s and c_2 for the (improved) rectangular LBE with $a=0.6$ are chosen as 0.44 and -2.8, respectively. The comparison results between the improved rectangular LBE and the previous one for the micro-lid-driven cavity flow are listed in Table 5. From the table it is shown that the differences of simulation results between the improved rectangular LBE and the previous one are negligibly small under the same values of c_s and c_2. Furthermore, the differences of simulation results between the improved rectangular LBE and the square LBE may mainly come from the differences of c_s and c_2 between the two models. This is because, the improved rectangular LBE is intrinsically a compressible scheme and the choice of c_s and c_2 can affect the values of the relaxation parameters, the speed of sound, viscosity, and combination parameters, which may lead to the differences of simulation results between the improved rectangular LBE and the square LBE. Table 6 shows the effect of the choice of c_s and c_2 on the computational efficiency and difference between the improved rectangular LBE and the square LBE. In addition, it is interesting to note that the RGD (E_u) of the improved rectangular LBE is slightly higher than that of the previous one. The possible reason for this is that the error due to the additional term $\mathbf{R}$ just reduces the differences of simulation results between the improved rectangular LBE and the square LBE. Overall, the simulation results with the improved rectangular LBE or the previous rectangular LBE agree well with each other, and with the results with the square LBE. Therefore, as an alternative and efficient method, both the improved rectangular LBE and the previous rectangular LBE can be used to simulate gaseous microscale flows in some cases.

https://doi.org/10.4208/aamm.2014.m672 Published online by Cambridge University Press

Table 5: Comparison results between the improved rectangular LBE and the rectangular LBE for the micro-lid-driven cavity flow with $Re=0.3$ and $Kn=0.01$.

Models	c_s	c_2	IN	ψ_{time}	E_u
Rectangular LBE	0.44	-2.8	73900	0.480	2.17×10^{-3}
Improved rectangular LBE	0.44	-2.8	73900	0.480	2.23×10^{-3}

Table 6: Effect of c_s and c_2 on the computational efficiency and difference between the improved rectangular LBE with $a=0.6$ and the square LBE for the micro-lid-driven cavity flow with $Re=0.3$ and $Kn=0.01$.

c_s	c_2	IN	ψ_{time}	E_u
0.40	-2.8	80000	0.520	1.74×10^{-3}
0.42	-2.8	77400	0.503	1.97×10^{-3}
0.44	-2.8	73900	0.480	2.23×10^{-3}
0.46	-2.8	70700	0.459	2.52×10^{-3}
0.46	-2.5	72800	0.473	3.33×10^{-3}

5 Summary

We have expanded the application scopes of the rectangular LBE model to gaseous microscale flow by choosing the suitable boundary conditions and the reasonable relationship between the relaxation parameter (s_8) and Kn. In particular, we have analyzed the discrete effects in the CBBSR and DMDR boundary conditions for the rectangular LBE with different values of the grid aspect ratio a in detail and have investigated the computational efficiency and difference between the rectangular LBE and the square LBE in several simulations. Some results are summarized as follows. First of all, the Chapman-Enskog analysis is used to derive the macroscopic equations from the rectangular LBE model presented in [26]. It is found that compared with the Navier-Stokes equations, the derived momentum equation includes an additional term which can be minimized or neglected in some cases. Second, the discrete forcing terms of the rectangular MRT-LBE model are directly chosen in moment space. We note that the discrete forcing terms in moment space suggested by us can make errors due to the discrete lattice effect of the external force disappear. Third, the relationship between s_8 and Kn for the rectangular LBE model depends on the choice of the rectangular grid, i.e., different values of the grid aspect ratio a result in different relationships. Fourth, some discrete effects exist in both the CBBSR and DMDR boundary conditions for the rectangular LBE. Therefore, a reasonable approach to determine the parameters r and σ in the two boundary conditions for the rectangular LBE is proposed. It is found that the real fully diffusive boundary condition can not be realized by the DMDR boundary condition in the square MRT-LBE, but can be implemented by the DMDR boundary condition in the rectangular LBE with a given value of $a\neq1$. The numerical simulations are implemented to validate the presented theoretical analysis. Finally, the computational efficiency and relative difference between the rectangular LBE and the square LBE in some simulations are analyzed in detail. It is found that the rectangular LBE is more efficient than the square LBE in simulating flows

https://doi.org/10.4208/aamm.2014.m672 Published online by Cambridge University Press

in domains with large aspect ratios under nearly the same accuracy. Consequently, the rectangular LBE, as an alternative and efficient approach, has advantages over the square LBE for simulating gaseous microscale flows in such cases.

Appendix: Chapman-Enskog analysis of the rectangular MRT-LBE

The density distribution function, the derivatives of time and space, and the external force can be expanded by a small parameter ε:

$$f_i = f_i^{(0)} + \varepsilon f_i^{(1)} + \varepsilon^2 f_i^{(2)} + \cdots, \tag{A.1a}$$

$$\partial_t = \varepsilon \partial_{t_0} + \varepsilon^2 \partial_{t_1}, \tag{A.1b}$$

$$\partial_\alpha = \varepsilon \partial_{0\alpha}, \tag{A.1c}$$

$$\mathbf{F} = \varepsilon \mathbf{F}_0, \tag{A.1d}$$

where $\mathbf{F}_0 = (F_{x0}, F_{y0})^{\mathrm{T}}$. Substituting the above Eqs. (A.1a)-(A.1d) into Eq. (2.1), we can obtain the zero-, first-, and second-order equations in ε:

$$\varepsilon^0 : f_i^{(0)} = f_i^{(\mathrm{eq})}, \tag{A.2a}$$

$$\varepsilon^1 : D_{0i} f_i^{(0)} = -\frac{1}{\delta_t} \sum_{j=0}^{8} (\mathbf{M}^{-1}\mathbf{S}\mathbf{M})_{ij} f_j^{(1)} + F'_{i0}, \tag{A.2b}$$

$$\varepsilon^2 : \partial_{t_1} f_i^{(0)} + D_{0i} f_i^{(1)} + \frac{\delta_t}{2} D_{0i}^2 f_i^{(0)} = -\frac{1}{\delta_t} \sum_{j=0}^{8} (\mathbf{M}^{-1}\mathbf{S}\mathbf{M})_{ij} f_j^{(2)}, \tag{A.2c}$$

where $D_{0i} = \partial_{t_0} + c_{i\alpha}\partial_{0\alpha}$ and $F'_i = \varepsilon F'_{i0}$.

Rewriting Eqs. (A.2a)-(A.2c) in vector form and multiplying the transformation matrix $\mathbf{M}$ on both sides of them, we can derive the corresponding equations in the moment space:

$$\varepsilon^0 : \mathbf{m}^{(0)} = \mathbf{m}^{(\mathrm{eq})}, \tag{A.3a}$$

$$\varepsilon^1 : \widehat{\mathbf{D}}_0 \mathbf{m}^{(0)} = -\mathbf{S}' \mathbf{m}^{(1)} + \widehat{\mathbf{F}}_0, \tag{A.3b}$$

$$\varepsilon^2 : \partial_{t_1} \mathbf{m}^{(0)} + \widehat{\mathbf{D}}_0 (\mathbf{I} - \frac{\mathbf{S}}{2}) \mathbf{m}^{(1)} + \frac{\delta_t}{2} \widehat{\mathbf{D}}_0 \widehat{\mathbf{F}}_0 = -\mathbf{S}' \mathbf{m}^{(2)}, \tag{A.3c}$$

where $\mathbf{m}^{(k)} = \mathbf{M}\mathbf{f}^{(k)}$, $\mathbf{f}^{(k)} = (f_0^{(k)}, f_1^{(k)}, \cdots, f_8^{(k)})^{\mathrm{T}}$, $\widehat{\mathbf{F}}_0 = \mathbf{M}\mathbf{F}'_0$, $\mathbf{F}'_0 = (F'_{00}, F'_{10}, \cdots, F'_{80})^{\mathrm{T}}$, $\mathbf{S}' = \mathbf{S}/\delta_t$, $\widehat{\mathbf{D}}_0 = \mathbf{M}\mathbf{D}_0\mathbf{M}^{-1}$, $\mathbf{D}_0 = \partial_{t_0}\mathbf{I} + \partial_{0\alpha}\mathrm{diag}(c_{0\alpha}, c_{1\alpha}, \cdots, c_{8\alpha})$, and $\mathbf{I}$ is the unit matrix.

Based on Eqs. (2.5a) and (2.5b), the elements of $\mathbf{m}^{(1)}$ corresponding to the conservative variables ρ and $\rho\mathbf{u}$ are zero and $-\delta_t\mathbf{F}_0/2$, respectively. Therefore, considering Eqs. (2.10a)-

https://doi.org/10.4208/aamm.2014.m672 Published online by Cambridge University Press

(2.10c), we can rewrite Eq. (A.3b) as

$$\partial_{t_0}\rho+\partial_{0x}(\rho u_x)+\partial_{0y}(\rho u_y)=0, \tag{A.4a}$$

$$\partial_{t_0}(\rho u_x)+\partial_{0x}(\rho c_s^2+\rho u_x^2)+\partial_{0y}(\rho u_x u_y)=F_{x0}, \tag{A.4b}$$

$$\partial_{t_0}(\rho u_y)+\partial_{0x}(\rho u_x u_y)+\partial_{0y}(\rho c_s^2+\rho u_y^2)=F_{y0}. \tag{A.4c}$$

Similarly, Eq. (A.3c) can be rewritten as

$$\partial_{t_1}\rho=0, \tag{A.5a}$$

$$\begin{aligned}&\partial_{t_1}(\rho u_x)-\frac{\delta_t}{2}\partial_{t_0}\left[\left(1-\frac{s_3}{2}\right)F_{x0}\right]+\frac{1}{3+3a^4}\left(1-\frac{s_1}{2}\right)\partial_{0x}e^{(1)}+\frac{a^2}{3+3a^4}\left(1-\frac{s_7}{2}\right)\partial_{0x}p_{xx}^{(1)}\\&+\left(1-\frac{s_8}{2}\right)\partial_{0y}p_{xy}^{(1)}+\frac{\delta_t}{2}\left\{\partial_{t_0}\left[\left(1-\frac{s_3}{2}\right)F_{x0}\right]+\partial_{0x}\left[\frac{6}{3+3a^4}\left(1-\frac{s_1}{2}\right)(u_xF_{x0}+u_yF_{y0})\right.\right.\\&\left.\left.+\frac{6a^2}{3+3a^4}\left(1-\frac{s_7}{2}\right)\left(a^2u_xF_{x0}-\frac{1}{a^2}u_yF_{y0}\right)\right]+\partial_{0y}\left[\left(1-\frac{s_8}{2}\right)(u_xF_{y0}+u_yF_{x0})\right]\right\}=0,\end{aligned} \tag{A.5b}$$

$$\begin{aligned}&\partial_{t_1}(\rho u_y)-\frac{\delta_t}{2}\partial_{t_0}\left[\left(1-\frac{s_5}{2}\right)F_{y0}\right]+\frac{a^4}{3+3a^4}\left(1-\frac{s_1}{2}\right)\partial_{0y}e^{(1)}-\frac{a^2}{3+3a^4}\left(1-\frac{s_7}{2}\right)\partial_{0y}p_{xx}^{(1)}\\&+\left(1-\frac{s_8}{2}\right)\partial_{0x}p_{xy}^{(1)}+\frac{\delta_t}{2}\left\{\partial_{t_0}\left[\left(1-\frac{s_5}{2}\right)F_{y0}\right]+\partial_{0x}\left[\left(1-\frac{s_8}{2}\right)(u_xF_{y0}+u_yF_{x0})\right]\right.\\&\left.+\partial_{0y}\left[\frac{6a^4}{3+3a^4}\left(1-\frac{s_1}{2}\right)(u_xF_{x0}+u_yF_{y0})-\frac{6a^2}{3+3a^4}\left(1-\frac{s_7}{2}\right)\left(a^2u_xF_{x0}-\frac{1}{a^2}u_yF_{y0}\right)\right]\right\}=0.\end{aligned} \tag{A.5c}$$

Neglecting the terms $\mathcal{O}(|\mathbf{u}|^3)$ as a small quantity under the incompressible condition and with the aid of Eq. (A.3b), we can derive the following equations for $e^{(1)}$, $p_{xx}^{(1)}$ and $p_{xy}^{(1)}$:

$$\begin{aligned}-s'_1e^{(1)}=&\frac{-12c_s^2+10+c_2}{2}\rho\partial_{0x}u_x+\frac{-12c_s^2+4+c_2+6a^2}{2}\rho\partial_{0y}u_y\\&+3s_1(u_xF_{x0}+u_yF_{y0}),\end{aligned} \tag{A.6a}$$

$$\begin{aligned}-s'_7p_{xx}^{(1)}=&-\frac{4+c_2-6c_s^2+6a^4(-1+c_s^2)}{2a^2}\rho\partial_{0x}u_x+\frac{-6a^2+6c_s^2+a^4(4+c_2-6c_s^2)}{2a^2}\rho\partial_{0y}u_y\\&+3s_7\left(a^2u_xF_{x0}-\frac{1}{a^2}u_yF_{y0}\right),\end{aligned} \tag{A.6b}$$

$$-s'_8p_{xy}^{(1)}=\frac{4+c_2}{6}\rho\partial_{0x}u_y+\frac{4+c_2}{6}\rho\partial_{0y}u_x+\frac{s_8}{2}(u_xF_{y0}+u_yF_{x0}). \tag{A.6c}$$

Substituting Eqs. (A.6a)-(A.6c) into Eqs. (A.5a)-(A.5c) and considering Eqs. (2.14a) and (2.14b), we derive the hydrodynamic equations in ε^2:

$$\partial_{t_1}\rho=0, \tag{A.7a}$$

$$\begin{aligned}\partial_{t_1}(\rho u_x)=&\partial_{0x}\left[\rho\zeta(\partial_{0x}u_x+\partial_{0y}u_y)\right]+\partial_{0x}\left[\rho\nu(\partial_{0x}u_x-\partial_{0y}u_y)\right]\\&+\partial_{0y}\left[\rho\nu(\partial_{0x}u_y+\partial_{0y}u_x)\right]+\frac{a^2-1}{2}\left(\frac{1}{s_1}-\frac{1}{2}\right)\delta_t\partial_{0x}(\rho\partial_{0y}u_y),\end{aligned} \tag{A.7b}$$

https://doi.org/10.4208/aamm.2014.m672 Published online by Cambridge University Press

$$\partial_{t_1}(\rho u_y)=\partial_{0y}\left[\rho\zeta(\partial_{0x}u_x+\partial_{0y}u_y)\right]+\partial_{0y}\left[\rho\nu(\partial_{0y}u_y-\partial_{0x}u_x)\right]$$
$$+\partial_{0x}\left[\rho\nu(\partial_{0x}u_y+\partial_{0y}u_x)\right]+\frac{1-a^2}{2}\left(\frac{1}{s_1}-\frac{1}{2}\right)\delta_t\partial_{0y}(\rho\partial_{0x}u_x), \tag{A.7c}$$

where ν and ζ are the kinematic shear and bulk viscosities given by

$$\nu=\frac{4+c_2}{6}\left(\frac{1}{s_8}-\frac{1}{2}\right)\delta_t, \tag{A.8a}$$
$$\zeta=\frac{1}{12}(7+3a^2+c_2-12c_s^2)\left(\frac{1}{s_1}-\frac{1}{2}\right)\delta_t. \tag{A.8b}$$

Finally, combining the results at the orders of ε and ε^2, we can obtain the following macroscopic equations:

$$\partial_t\rho+\nabla\cdot(\rho\mathbf{u})=0, \tag{A.9a}$$
$$\partial_t(\rho\mathbf{u})+\nabla\cdot(\rho\mathbf{u}\mathbf{u})=-\nabla p+\nabla\cdot[\rho\nu(\nabla\mathbf{u}+(\nabla\mathbf{u})^{\mathrm{T}}-(\nabla\cdot\mathbf{u})\mathbf{I})+\rho\zeta(\nabla\cdot\mathbf{u})\mathbf{I}]+\mathbf{F}+\mathbf{R}, \tag{A.9b}$$

where $p=\rho c_s^2$ is the pressure, $\mathbf{u}=(u_x,u_y)^{\mathrm{T}}$, $\mathbf{F}=(F_x,F_y)^{\mathrm{T}}$ and the additional term $\mathbf{R}$ is given as follows

$$\mathbf{R}=\left[\frac{a^2-1}{2}\left(\frac{1}{s_1}-\frac{1}{2}\right)\delta_t\partial_x(\rho\partial_y u_y),\ \frac{1-a^2}{2}\left(\frac{1}{s_1}-\frac{1}{2}\right)\delta_t\partial_y(\rho\partial_x u_x)\right]^{\mathrm{T}}. \tag{A.10}$$

Acknowledgements

J. J. Ren would like to thank Professor Pierre Lallemand for many helpful discussions via email. P. Guo would like to acknowledge the support by the National Natural Science Foundation of China (No. 51204141). Z. L. Guo would like to acknowledge the support by the National Natural Science Foundation of China (No. 51125024) and the National Basic Research Programme of China (No. 2011CB707305).

References

[1] C. M. Ho and Y. C. Tai, *Micro-electro-mechanical-systems (MEMS) and fluid flows,* Annu. Rev. Fluid Mech., 30 (1998), pp. 579–612.
[2] G. E. Karniadakis and A. Beskok, Micro Flows: Fundamentals and Simulation, Springer, New York, 2002.
[3] X. He and L. S. Luo, *Theory of the lattice Boltzmann method: from the Boltzmann equation to the lattice Boltzmann equation,* Phys. Rev. E, 56 (1997), pp. 6811–6817.
[4] X. Shan and X. He, *Discretization of the velocity space in the solution of the Boltzmann equation,* Phys. Rev. Lett., 80 (1998), pp. 65–68.
[5] C. K. Aidun and J. R. Clausen, *Lattice-Boltzmann method for complex flows,* Annu. Rev. Fluid Mech., 42 (2010), pp. 439–472.

https://doi.org/10.4208/aamm.2014.m672 Published online by Cambridge University Press

[6] X. Nie, G. D. Doolen and S. Chen, *Lattice-Boltzmann simulations of fluid flows in MEMS,* J. Stat. Phys., 107 (2002), pp. 279–289.
[7] C. Y. Lim, C. Shu, X. D. Niu and Y. T. Chew, *Application of lattice Boltzmann method to simulate microchannel flows,* Phys. Fluids, 14 (2002), pp. 2299–2308.
[8] A. Agrawal, L. Djenidi and R. A. Antonia, *Simulation of gas flow in microchannels with a sudden expansion or contraction,* J. Fluid Mech., 530 (2005), pp. 135–144.
[9] T. Lee and C. L. Lin, *Rarefaction and compressibility effects of the lattice- Boltzmann-equation method in a gas microchannel,* Phys. Rev. E, 71 (2005), 046706.
[10] M. Sbragaglia and S. Succi, *Analytical calculation of slip flow in lattice Boltzmann models with kinetic boundary conditions,* Phys. Fluids, 17 (2005), 093602.
[11] G. H. Tang, W. Q. Tao and Y. L. He, *Lattice Boltzmann method for gaseous microflows using kinetic theory boundary conditions,* Phys. Fluids, 17 (2005), 058101.
[12] Y. H. Zhang, R. Qin and D. R. Emerson, *Lattice Boltzmann simulation of rarefied gas flows in microchannels,* Phys. Rev. E, 71 (2005), 047702.
[13] Y. H. Zhang, X. J. Gu, R. W. Barber and D. R. Emerson, *Capturing Knudsen layer phenomena using a lattice Boltzmann model,* Phys. Rev. E, 74 (2006), 046704.
[14] Z. L. Guo, T. S. Zhao and Y. Shi, *Physical symmetry, spatial accuracy, and relaxation time of the lattice Boltzmann equation for microgas flows*, J. Appl. Phys., 99 (2006), 074903.
[15] Z. L. Guo, B. C. Shi, T. S. Zhao and C. G. Zheng, *Discrete effects on boundary conditions for the lattice Boltzmann equation in simulating microscale gas flows,* Phys. Rev. E, 76 (2007), 056704.
[16] Z. L. Guo, C. G. Zheng and B. C. Shi, *Lattice Boltzmann equation with multiple effective relaxation times for gaseous microscale flow,* Phys. Rev. E, 77 (2008), 036707.
[17] Z. L. Guo and C. G. Zheng, *Analysis of lattice Boltzmann equation for microscale gas flows: relaxation times, boundary conditions and the Knudsen layer,* Int. J. Comput. Fluid Dyn., 22 (2008), pp. 465–473.
[18] L. Zheng, Z. L. Guo and B. C. Shi, *Discrete effects on thermal boundary conditions for the thermal lattice Boltzmann method in simulating microscale gas flows,* Europhys. Lett., 82 (2008), 44002.
[19] Z. L. Guo, P. Asinari and C. G. Zheng, *Lattice Boltzmann equation for microscale gas flows of binary mixtures*, Phys. Rev. E, 79 (2009), 026702.
[20] F. Verhaeghe, L. S. Luo and B. Blanpain, *Lattice Boltzmann modeling of microchannel flow in slip flow regime,* J. Comput. Phys., 228 (2009), pp. 147–157.
[21] Y. Shi and J. E. Sader, *Lattice Boltzmann method for oscillatory Stokes flow with applications to micro- and nanodevices,* Phys. Rev. E, 81 (2010), 036706.
[22] L. Zheng, Z. L. Guo and B. C. Shi, *Microscale boundary conditions of the lattice Boltzmann equation method for simulating microtube flows,* Phys. Rev. E, 86 (2012), 016712.
[23] X. L. Liu and Z. L. Guo, *A lattice Boltzmann study of gas flows in a long micro-channel,* Comput. Math. Appl., 65 (2013), pp. 186–193.
[24] C. Zhuo and C. Zhong, *Filter-matrix lattice Boltzmann model for microchannel gas flows,* Phys. Rev. E, 88 (2013), 053311.
[25] T. M. Liou and C. T. Lin, *Study on microchannel flows with a sudden contraction-expansion at a wide range of Knudsen number using lattice Boltzmann method,* Microfluid Nanofluid, 16 (2014), pp. 315–327.
[26] M. Bouzidi, D. d'Humières, P. Lallemand and L. S. Luo, *Lattice Boltzmann equation on a two-dimensional rectangular grid,* J. Comput. Phys., 172 (2001), pp. 704–717.
[27] J. G. Zhou, *Rectangular lattice Boltzmann method*, Phys. Rev. E, 81 (2010), 026705.
[28] S. Chikatamarla and I. Karlin, *Comment on "Rectangular lattice Boltzmann method",*

https://doi.org/10.4208/aamm.2014.m672 Published online by Cambridge University Press

Phys. Rev. E, 83 (2011), 048701.
[29] J. G. ZHOU, *MRT rectangular lattice Boltzmann method,* Int. J. Mod. Phys. C, 23 (2012), 1250040.
[30] L. A. HEGELE JR, K. MATTILA AND P. C. PHILIPPI, *Rectangular lattice-Boltzmann schemes with BGK-collision operator,* J. Sci. Comput., 56 (2013), pp. 230–242.
[31] X. HE, L. S. LUO AND M. DEMBO, *Some progress in lattice Boltzmann method, Part I. nonuniform mesh grids,* J. Comput. Phys., 129 (1996), pp. 357–363.
[32] Z. CHAI AND T. S. ZHAO, *Effect of the forcing term in the multiple-relaxation-time lattice Boltzmann equation on the shear stress or the strain rate tensor*, Phys. Rev. E, 86 (2012), 016705.
[33] C. CERCIGNANI, Mathematical Methods in Kinetic Theory, Plenum Press, New York, 1990.
[34] S. SUCCI, *Mesoscopic modeling of slip motion at fluid-solid interfaces with heterogeneous catalysis*, Phys. Rev. Lett., 89 (2002), 064502.
[35] S. ANSUMALI AND I. V. KARLIN, *Kinetic boundary conditions in the lattice Boltzmann method*, Phys. Rev. E, 66 (2002), 026311.
[36] C. SHEN, D. B. TIAN, C. XIE AND J. FAN, *Examination of the LBM in simulation of microchannel flow in transitional regime,* Microscale Thermophys. Eng., 8 (2004), pp. 423–432.
[37] J. A. ESFAHANI AND A. NOROUZI, *Two relaxation time lattice Boltzmann model for rarefied gas flows*, Phys. A, 393 (2014), pp. 51–61.
[38] C. ZHUO AND C. ZHONG, *Filter-matrix lattice Boltzmann model for microchannel gas flows,* Phys. Rev. E, 88 (2013), 053311.

https://doi.org/10.4208/aamm.2014.m672 Published online by Cambridge University Press